Electronic Supplementary Material (ESI) for Physical Chemistry Chemical Physics.

Supporting Information

Plasmonic Properties of Regiospecific Core-Satellite Assemblies of Gold Nanostars and Nanospheres

*A. Swarnapali D. S. Indrasekara, Roney Thomas and Laura Fabris**

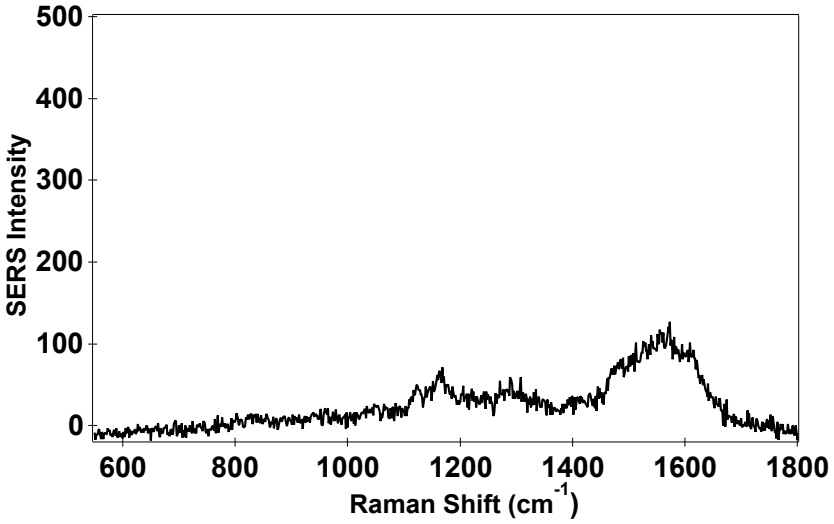

Figure S1. Residual ascorbic acid molecules are present on the surface of purified STs. SERS spectrum of purified STs collected at 785 nm (diode laser, 1mW, 15 s exposure, 2 accumulations).

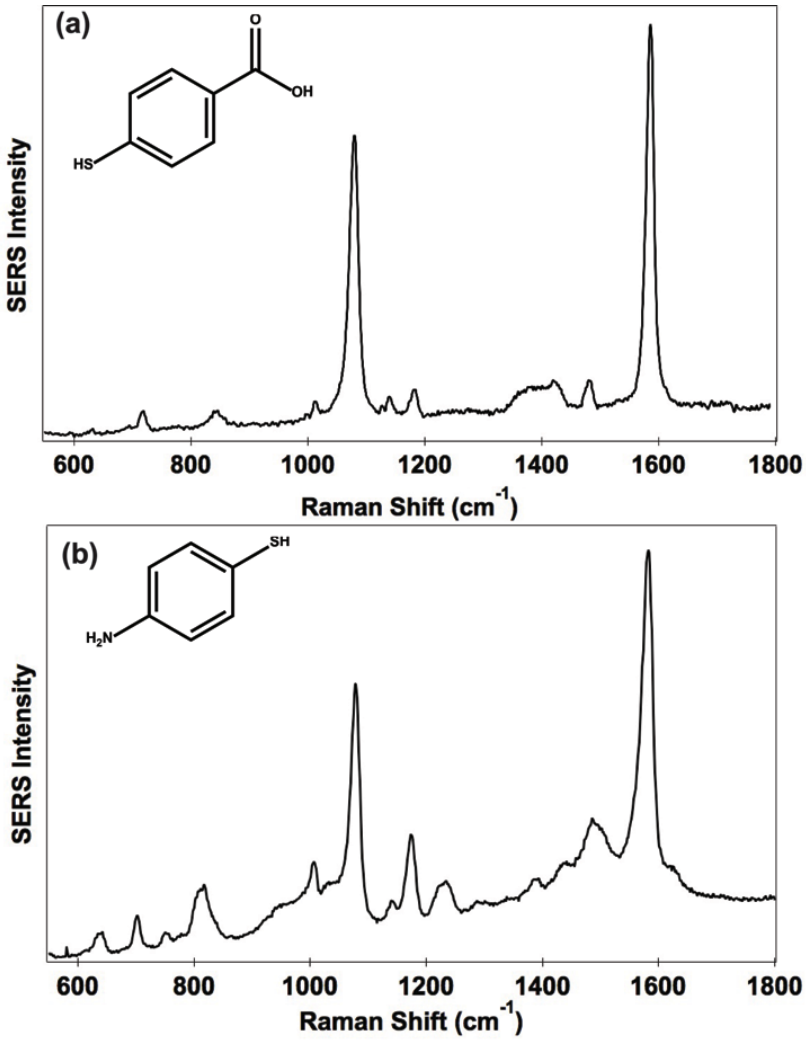

Figure S2. The presence of characteristic SERS spectra confirms the successful ligand exchange of STs and SPs with 4-MBA and 4-ATP, respectively. SERS spectra of (a) 4-MBA-capped STs, and (b) 4-ATP-capped SP. SERS spectra were acquired under 785 nm diode laser excitation (1 mW, 15 s exposure, 2 accumulations).

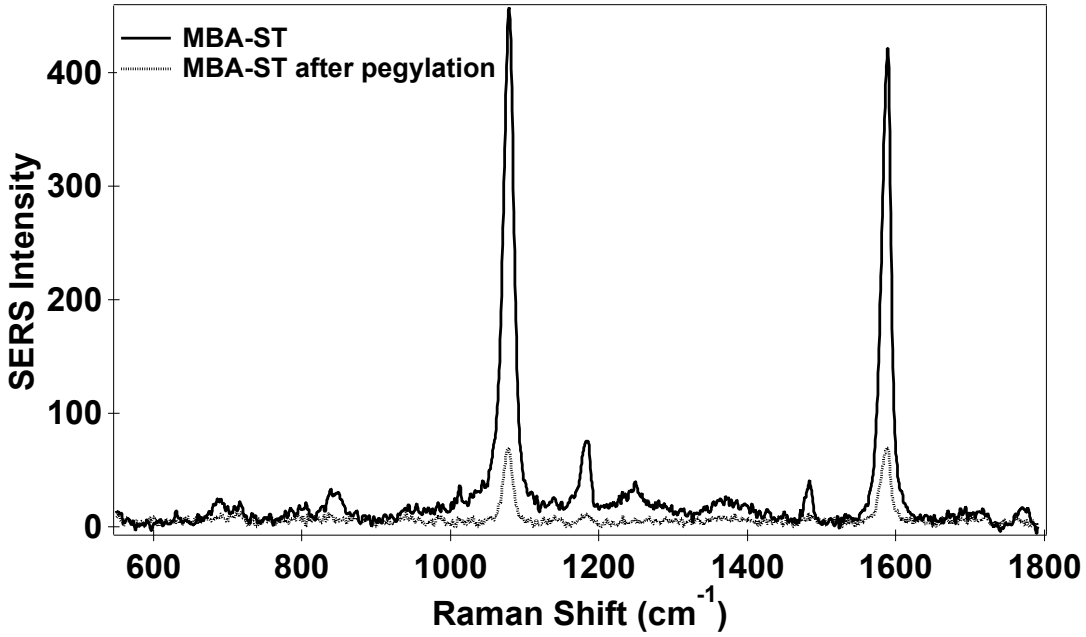

Figure S3. Intensity of the MBA-ST SERS signal decreases by a factor of 11 upon pegylation carried out overnight. This supports the fact that a significant amount of 4-MBA on ST is replaced by MeO-PEG-SH. The SERS spectra shown were acquired under 785 nm diode laser excitation (1mW, 15 s exposure, 2 accumulations) for 5 μL, 13 pM and 10 μL, 13 pM MBA-ST and pegylated MBA-ST respectively. Both MBA-ST and pegylated MBA-ST were purified by centrifugation, resuspended in MilliQ water and then used for the SERS analysis.

Optimization of the Core-Satellite Assembly

Both the preparation of EDC/sulfo-NHS solutions and the assembly reactions were carried out in MilliQ water at pH 6-7 and room temperature. Early attempts to EDC/sulfo-NHS cross-linking reactions were carried out in Tris-borate, phosphate, and MES buffers, but the TEM analysis revealed morphology changes of NPs, which could most probably be due to the buffers (**Figure S4a**). As the reaction medium was changed to MilliQ water at neutral pH no such behavior was observed, hence this condition was used for all the assembly reactions reported here.

Different molar ratios of MBA-ST to ATP-SP ranging from (1:10 to 1:200) were examined to determine the optimum conditions for the assembly reaction. Based on TEM and absorption spectra, it was concluded that ATP-SP to MBA-ST molar ratios above 1:50 result in a higher yield of assembly, i.e. a higher number of satellite NPs (SPs) per core NP (ST). At molar ratios above 1:50, excess SPs as well as aggregated assemblies were observed, which could be attributed to the reaction between 4-ATP on excess SPs with the activated 4-MBA on STs which then led to further assembly in even larger ST-SP superstructures. At molar ratios below 1:50, the yield of SP satellites bound per core STs was close to zero. At both these extremes, the absorption spectra of the assemblies resembled the dominant precursor NP and no spectral changes were observed. Thus, for the further optimization of the assembly scheme, a ST:SP 1:50 molar ratio was considered.

In order to eliminate the assembly of ST-SP due to the capillary forces during the TEM sample preparation as well as due to any possible electrostatic or hydrogen bonding interaction among the NPs, a mixture of MBA-ST to ATP-SP at 1:50 molar ratio without EDC/sulfo-NHS coupling reaction was analyzed by TEM and UV-VIS spectroscopy. Unlike the samples under the assembly condition, the control sample didn't exhibit any spectral changes in the absorption spectrum or core-satellite type assemblies in TEM micrographs (**Figure S4b**). Therefore the observed core-satellite assemblies on TEM can be attributed due to the EDC/sulfo-NHS cross-linking reactions.

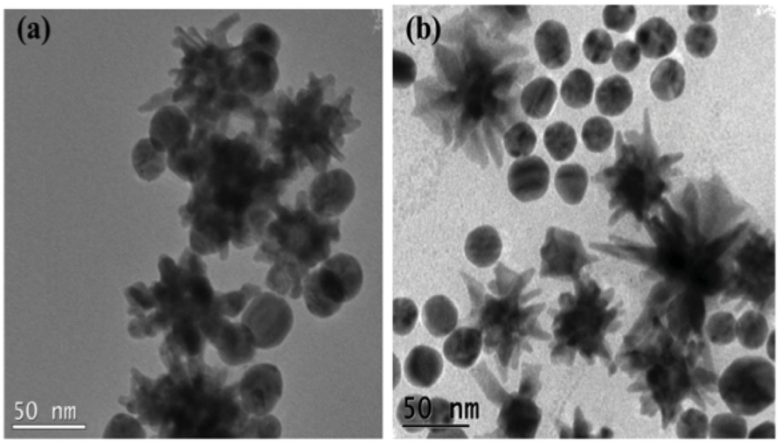

Figure S4. TEM micrographs of (a) ST-SP assembly in borate buffer, and (b) ST-SP mixture without coupling reagents. Significant changes in the morphology of STs can be observed in borate buffer. In the absence of EDC/sulfo-NHS linkers, no core satellite assembly takes place.

Core-Satellite Assembly Using 12 nm Gold Nanospheres

The same assembly scheme followed for gold nanospheres of 24 nm in diameter was used to carry out assembly experiments with satellite spheres with diameters of 12 nm. Core–satellite assemblies of ST:SP molar ratio of 1: 50, 1:100, 1:150 and 1:200 were carried out, their optical properties were characterized by absorption and SERS spectra, and imaged by TEM microscopy (**Figure S5**). The assemblies exhibited similar spectral changes in the absorption spectra seen with 24 nm SPs, thereby providing evidence of plasmon coupling mediated by NP assembly. The TEM micrographs show SPs with diameter of 12 nm assembled over the spikes of STs with narrow interparticle gaps (< 2 nm). Even in the presence of multiple SP assemblies per ST (much higher than that with 24 nm SPs), the observed SERS enhancement is not significant. This could be explained as due to the smaller size of the SPs, which contributes to the plasmon coupling with STs to a lower extent. Even though the SP-ST assembly with 12 nm SPs results in SERS

enhancement higher than the constituent nanoparticles (by an order of magnitude), it is not as significant as that achieved using 24 nm SPs.

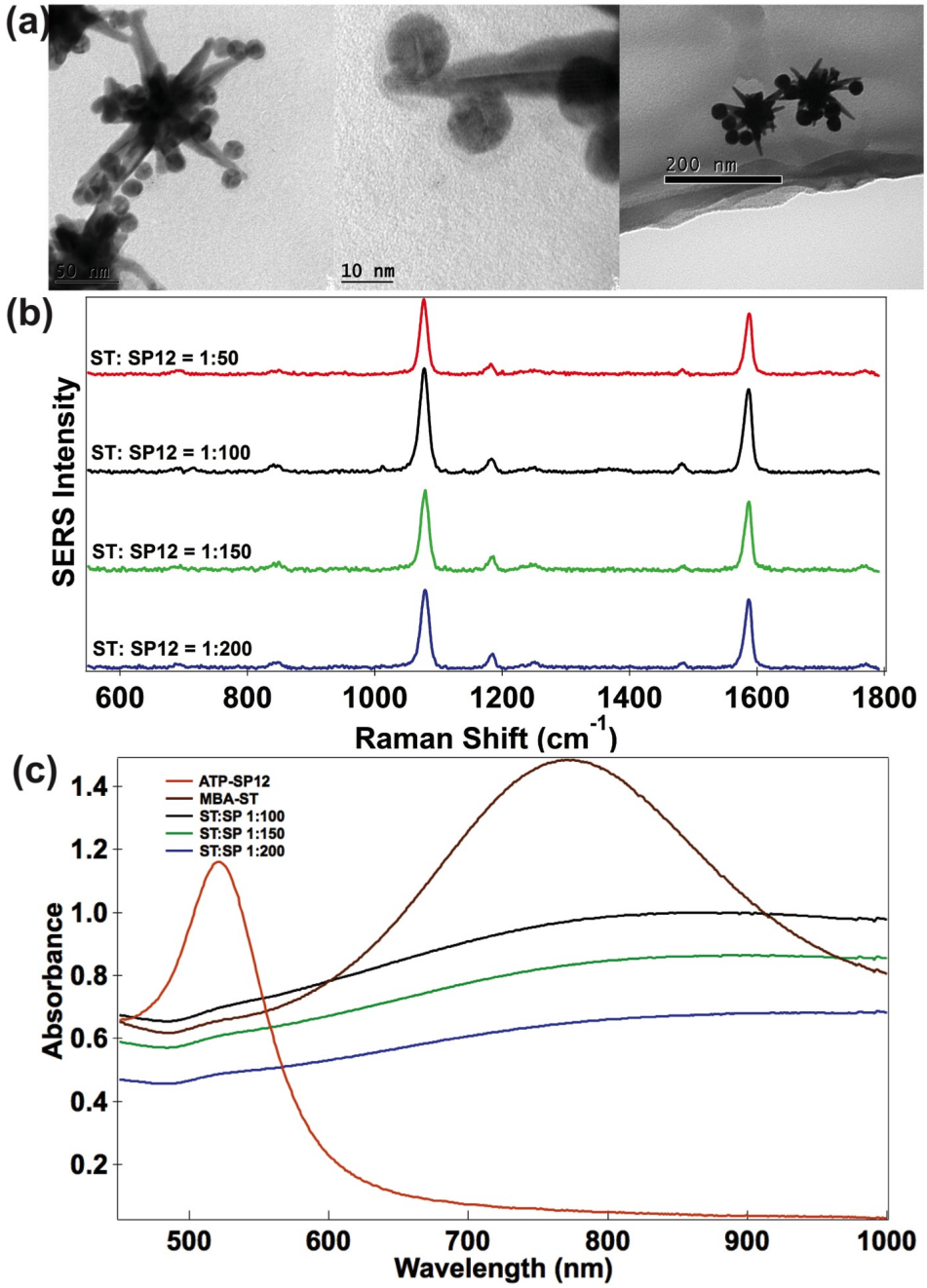

Figure S5. SPs with diameters of 12 nm (SP12) assemble over the spikes of STs creating narrow interparticle gaps (< 2nm), and thereby resulting in average one order of magnitude increase in the SERS activity compared to precursor STs. (a) TEM micrographs of SP12-ST core satellite assemblies, (b) SERS spectra, and (c) the absorption spectra of SP12-ST assemblies at different molar ratios.

2D-FEEM Simulations

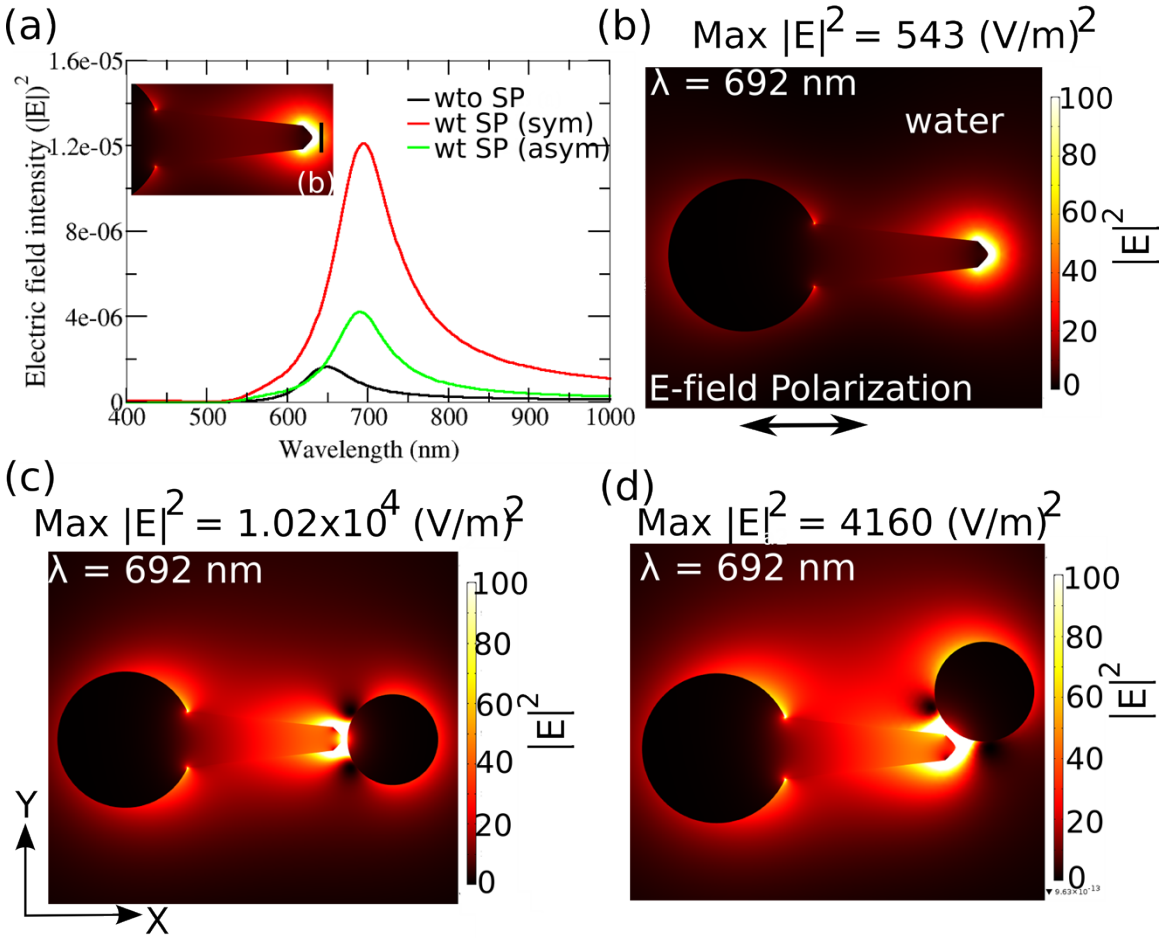

Figure S6. (a) $|E|^2$ spectra integrated over a 10 nm line (see inset) for the ST structures with configurations shown in (b), (c), and (d). Electric field intensity ($|E|^2$) plots at λ = 692 nm, when a normally incident TM polarized light (i.e. E-field polarized along the X-axis) illuminates a ST structure comprising of (b) a single protruding spike, (c) a single protruding spike and a SP situated symmetrically at 1.28 nm away from the tip of the spike, and (d) with a spike and a SP situated asymmetrically with respect to the axis of the protruding spike, wherein the separation of SP from the slant edge of the spike is kept approximately constant (i.e. ~ 1.28 nm). Indicated, for b), c), and d) are also the maximum electric field intensities $|E|^2$ for each configuration.

The effect of increasing the number of protruding spikes on the magnitude and behavior of the electric field intensity near the tip of the spike was studied using 2D FEEM simulations. The integrated $|E|^2$ spectra were calculated as previously described and are reported in Fig. S7. The figure predicts the ensuance of multiple peaks in the $|E|^2$

spectrum as the number of spikes increases. For the ST with two spikes, two $|E|^2$ maxima at λ = 600 nm and 780 nm and a minimum at λ = 725 nm can be observed. To understand the nature of the maxima and minimum, electric field intensity plots at wavelengths corresponding to these peak positions were obtained. Fig. S7b-d show the integrated $|E|^2$ plots for the gold ST with two protruding spikes at λ = 600 nm, 727 nm, and 775 nm, respectively. For ease of analysis, we have numbered (i.e. one, two, etc.) the spikes as they appear in anti-clockwise direction. Additionally, the region where the inner edges of the first and second spikes converge has been marked with a dotted circle (apex) in Fig. S7b. Careful observation of the figure shows a strong electric field intensity envelop that surrounds the two protruding spikes, as well as the region surrounding the central spherical core, which is also clearly evident in Fig. S7d. The field intensity appears to be strongly localized within the apex region of the converging spikes and to rapidly decay away from it. The enhanced $|E|^2$ in the vicinity of the apex between the converging spikes results from the spatial EM coupling between the plasmon modes excited by the tips of the two protruding spikes (i.e., spikes numbered 1 and 2), which becomes even more pronounced at resonance (i.e. for λ = 600 nm and 775 nm). Furthermore, Fig. S7b and d show strongly localized $|E|^2$ near the vicinity of the spherical tips of the first and second spikes, which can be attributed to resonant excitation of plasmon modes by the tips which, in turn, contribute towards localization of the $|E|^2$ and, therefore, result in two $|E|^2$ maxima at λ = 600 nm and 775 nm, as shown in Fig. S8a. In contrast, at λ = 727 nm, the plasmon mode of the first spike is weakly excited, which leads to a significantly reduced field intensity in the region in its close proximity, resulting in a minimum in the integrated electric field intensity at λ = 727 nm and contributing towards weak

localization of the field intensity near the apex region between the first and second spike.

Fig. S7e and f show the $|E|^2$ distribution for gold STs with three and six protruding spikes at wavelengths of 685 nm and 704 nm, which correspond to the peak field intensities shown by the green and blue spectra in Fig. S7a, respectively. The spikes protruding from the core of the ST have been numbered in anti-clockwise direction. In both figures, a strong intensity envelope surrounding the second and third spikes and the region between them can be observed. When these structures are illuminated from a TM polarized light (i.e. polarized along the X-axis), an increased spatial interaction between the incident light and the second and third protruding spikes leads to stronger excitation of the plasmon modes supported by the tips of the spikes in comparison to the plasmon mode excitation by the spherical tip of the first spike. This, in turn, leads to an even stronger EM coupling between the plasmon modes supported by the spikes, which results in a larger enhancement of the electric field intensity in the region between the second and third spike than in the region between the first and second spike. Additionally, the strong EM coupling between the plasmon modes leads to enhanced field intensity near the apex region where the second and third spikes converge, which is significantly larger than the corresponding position between spikes 1 and 2. In analogy to what discussed before, reduced spatial electromagnetic interaction of the incident light with the fifth and sixth spikes leads to a weakly excited plasmon mode by the tip of the spikes and, therefore, results in significantly reduced field intensity in proximity to the corresponding tips. Furthermore, it is interesting to observe that the integrated $|E|^2$ spectra show broader electric field intensity peaks for STs with three and six protruding spikes in comparison to the $|E|^2$ resonant peaks obtained for ST with one and two protruding spikes (see Fig.

S7a). The broadening of the resonance could be attributed to the contribution of the plasmon modes excited by the individual spikes from the core of the ST with three or more protruding spikes.

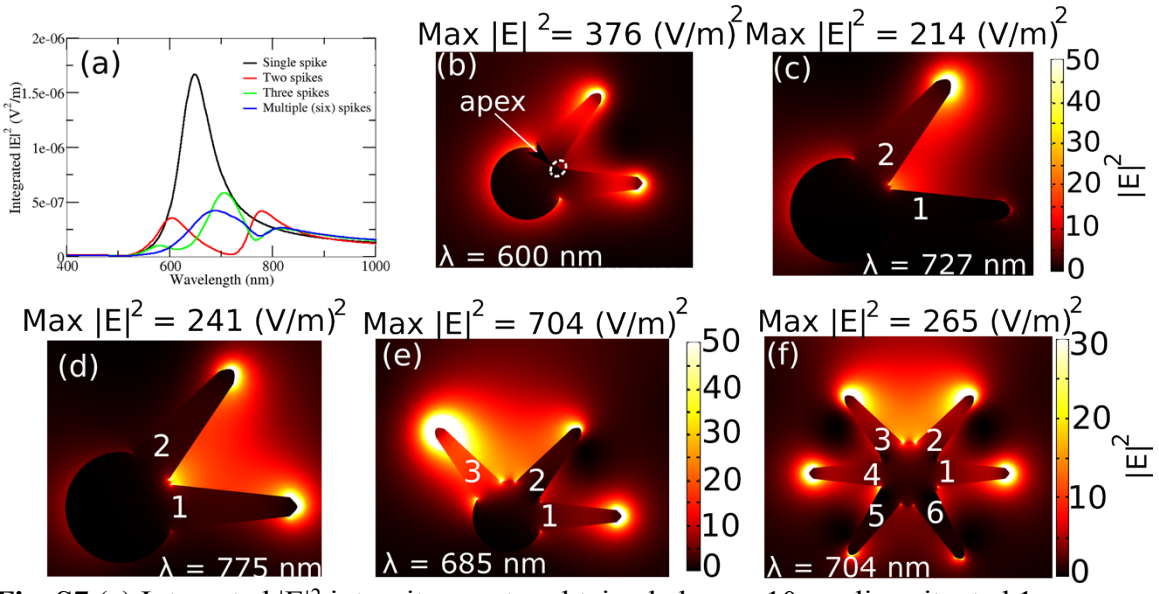

Fig. S7 (a) Integrated $|E|^2$ intensity spectra obtained along a 10 nm line situated 1 nm from the horizontally protruding spike 1. (b)-(d) $|E|^2$ intensity distribution for a ST with two protruding spikes at different wavelengths. The figures are scaled to the same magnitude as shown in the bar graph at right. (e)-(f) $|E|^2$ intensity distribution for a ST with three and six protruding spikes at $\lambda = 685$ nm and $\lambda = 704$ nm, respectively, which correspond to the $|E|^2$ intensity maxima.